

A Deeper Look at DES Dwarf Galaxy Candidates: Grus I and Indus II

SARAH A. CANTU,^{1,2} ANDREW B. PACE,^{3,1,2} JENNIFER MARSHALL,^{1,2} LOUIS E. STRIGARI,^{1,2} DENIJA CRNOJEVIC,⁴
JOSHUA D. SIMON,⁵ A. DRLICA-WAGNER,^{6,7,8} K. BECHTOL,^{9,10} CLARA E. MARTÍNEZ-VÁZQUEZ,¹¹ B. SANTIAGO,^{12,13}
A. AMARA,¹⁴ K. M. STRINGER,^{1,2} H. T. DIEHL,¹⁵ M. AGUENA,^{16,17} S. ALLAM,¹⁵ S. AVILA,¹⁸ D. BROOKS,¹⁹
A. CARNERO ROSELL,^{20,21} M. CARRASCO KIND,^{22,23} J. CARRETERO,²⁴ M. COSTANZI,^{25,26} L. N. DA COSTA,^{17,21}
J. DE VICENTE,²⁷ S. DESAI,²⁸ P. DOEL,¹⁹ T. F. EIFLER,^{29,30} S. EVERETT,³¹ J. FRIEMAN,^{15,7} J. GARCÍA-BELLIDO,¹⁸
E. GAZTANAGA,^{32,33} D. GRUEN,^{34,35,36} R. A. GRUENDL,^{22,23} J. GSCHWEND,^{17,21} G. GUTIERREZ,¹⁵ S. R. HINTON,³⁷
D. L. HOLLOWOOD,³¹ K. HONSCHIED,^{38,39} D. J. JAMES,⁴⁰ K. KUEHN,^{41,42} M. A. G. MAIA,^{17,21} F. MENANTEAU,^{22,23}
R. MIQUEL,^{43,24} A. PALMESE,^{15,7} F. PAZ-CHINCHÓN,^{44,23} A. A. PLAZAS,⁴⁵ E. SANCHEZ,²⁷ V. SCARPINE,¹⁵ M. SCHUBNELL,⁴⁶
S. SERRANO,^{32,33} I. SEVILLA-NOARBE,²⁷ M. SMITH,⁴⁷ M. SOARES-SANTOS,⁴⁸ E. SUCHYTA,⁴⁹ M. E. C. SWANSON,²³
G. TARLE,⁴⁶ A. R. WALKER,⁵⁰ AND R.D. WILKINSON⁵¹
(DES COLLABORATION)

¹George P. and Cynthia Woods Mitchell Institute for Fundamental Physics and Astronomy, Texas A&M University, College Station, TX 77843, USA

²Department of Physics & Astronomy, Texas A&M University, 4242 TAMU, College Station, TX 77843, USA

³McWilliams Center for Cosmology, Carnegie Mellon University, 5000 Forbes Ave., Pittsburgh, PA 15213, USA

⁴Department of Chemistry and Physics, University of Tampa, Tampa, FL, USA

⁵Observatories of the Carnegie Institution for Science, 813 Santa Barbara St., Pasadena, CA 91101, USA

⁶Fermi National Accelerator Laboratory, P.O. Box 500, Batavia, IL 60510, USA

⁷Kavli Institute for Cosmological Physics, University of Chicago, Chicago, IL 60637, USA

⁸Department of Astronomy and Astrophysics, University of Chicago, Chicago, IL 60637, USA

⁹Physics Department, 2320 Chamberlin Hall, University of Wisconsin-Madison, 1150 University Avenue Madison, WI 53706-1390

¹⁰LSST, 933 North Cherry Avenue, Tucson, AZ 85721, USA

¹¹Cerro Tololo Inter-American Observatory, NSF's National Optical-Infrared Astronomy Research Laboratory, Casilla 603, La Serena, Chile

¹²Instituto de Física, UFRGS, caixa Postal 15051, Porto Alegre, RS-91501-970, Brazil

¹³Laboratório Interinstitucional de e-Astronomia - LIneA, Rua Gal. José Cristino 77, Rio de Janeiro, RJ - 20921-400, Brazil

¹⁴Department of Physics, ETH Zurich, Wolfgang-Pauli-Strasse 16, CH-8093 Zurich, Switzerland

¹⁵Fermi National Accelerator Laboratory, P. O. Box 500, Batavia, IL 60510, USA

¹⁶Departamento de Física Matemática, Instituto de Física, Universidade de São Paulo, CP 66318, São Paulo, SP, 05314-970, Brazil

¹⁷Laboratório Interinstitucional de e-Astronomia - LIneA, Rua Gal. José Cristino 77, Rio de Janeiro, RJ - 20921-400, Brazil

¹⁸Instituto de Física Teórica UAM/CSIC, Universidad Autónoma de Madrid, 28049 Madrid, Spain

¹⁹Department of Physics & Astronomy, University College London, Gower Street, London, WC1E 6BT, UK

²⁰Laboratório Interinstitucional de e-Astronomia - LineA, Rua Gal. José Cristino 77, Rio de Janeiro, RJ - 20921-400, Brazil

²¹Observatório Nacional, Rua Gal. José Cristino 77, Rio de Janeiro, RJ - 20921-400, Brazil

²²Department of Astronomy, University of Illinois at Urbana-Champaign, 1002 W. Green Street, Urbana, IL 61801, USA

²³National Center for Supercomputing Applications, 1205 West Clark St., Urbana, IL 61801, USA

²⁴Institut de Física d'Altes Energies (IFAE), The Barcelona Institute of Science and Technology, Campus UAB, 08193 Bellaterra (Barcelona) Spain

²⁵INAF-Osservatorio Astronomico di Trieste, via G. B. Tiepolo 11, I-34143 Trieste, Italy

²⁶Institute for Fundamental Physics of the Universe, Via Beirut 2, 34014 Trieste, Italy

²⁷Centro de Investigaciones Energéticas, Medioambientales y Tecnológicas (CIEMAT), Madrid, Spain

²⁸Department of Physics, IIT Hyderabad, Kandi, Telangana 502285, India

²⁹Department of Astronomy/Steward Observatory, University of Arizona, 933 North Cherry Avenue, Tucson, AZ 85721-0065, USA

³⁰Jet Propulsion Laboratory, California Institute of Technology, 4800 Oak Grove Dr., Pasadena, CA 91109, USA

³¹Santa Cruz Institute for Particle Physics, Santa Cruz, CA 95064, USA

³²Institut d'Estudis Espacials de Catalunya (IEEC), 08034 Barcelona, Spain

³³Institute of Space Sciences (ICE, CSIC), Campus UAB, Carrer de Can Magrans, s/n, 08193 Barcelona, Spain

³⁴Department of Physics, Stanford University, 382 Via Pueblo Mall, Stanford, CA 94305, USA

³⁵*Kavli Institute for Particle Astrophysics & Cosmology, P. O. Box 2450, Stanford University, Stanford, CA 94305, USA*

³⁶*SLAC National Accelerator Laboratory, Menlo Park, CA 94025, USA*

³⁷*School of Mathematics and Physics, University of Queensland, Brisbane, QLD 4072, Australia*

³⁸*Center for Cosmology and Astro-Particle Physics, The Ohio State University, Columbus, OH 43210, USA*

³⁹*Department of Physics, The Ohio State University, Columbus, OH 43210, USA*

⁴⁰*Center for Astrophysics | Harvard & Smithsonian, 60 Garden Street, Cambridge, MA 02138, USA*

⁴¹*Australian Astronomical Optics, Macquarie University, North Ryde, NSW 2113, Australia*

⁴²*Lowell Observatory, 1400 Mars Hill Rd, Flagstaff, AZ 86001, USA*

⁴³*Institució Catalana de Recerca i Estudis Avançats, E-08010 Barcelona, Spain*

⁴⁴*Institute of Astronomy, University of Cambridge, Madingley Road, Cambridge CB3 0HA, UK*

⁴⁵*Department of Astrophysical Sciences, Princeton University, Peyton Hall, Princeton, NJ 08544, USA*

⁴⁶*Department of Physics, University of Michigan, Ann Arbor, MI 48109, USA*

⁴⁷*School of Physics and Astronomy, University of Southampton, Southampton, SO17 1BJ, UK*

⁴⁸*Brandeis University, Physics Department, 415 South Street, Waltham MA 02453*

⁴⁹*Computer Science and Mathematics Division, Oak Ridge National Laboratory, Oak Ridge, TN 37831*

⁵⁰*Cerro Tololo Inter-American Observatory, National Optical Astronomy Observatory, Casilla 603, La Serena, Chile*

⁵¹*Department of Physics and Astronomy, Pevensey Building, University of Sussex, Brighton, BN1 9QH, UK*

(Received May 8, 2020)

Submitted to ApJ

ABSTRACT

We present deep g - and r -band Magellan/Megacam photometry of two dwarf galaxy candidates discovered in the Dark Energy Survey (DES), Grus I and Indus II (DES J2038–4609). For the case of Grus I, we resolved the main sequence turn-off (MSTO) and ~ 2 mags below it. The MSTO can be seen at $g_0 \sim 24$ with a photometric uncertainty of 0.03 mag. We show Grus I to be consistent with an old, metal-poor (~ 13.3 Gyr, $[\text{Fe}/\text{H}] \sim -1.9$) dwarf galaxy. We derive updated distance and structural parameters for Grus I using this deep, uniform, wide-field data set. We find an azimuthally averaged half-light radius more than two times larger ($\sim 151_{-31}^{+21}$ pc; $\sim 4.16_{-0.74}^{+0.54}$) and an absolute V -band magnitude ~ -4.1 that is ~ 1 magnitude brighter than previous studies. We obtain updated distance, ellipticity, and centroid parameters which are in agreement with other studies within uncertainties. Although our photometry of Indus II is $\sim 2 - 3$ magnitudes deeper than the DES Y1 Public release, we find no coherent stellar population at its reported location. The original detection was located in an incomplete region of sky in the DES Y2Q1 data set and was flagged due to potential blue horizontal branch member stars. The best fit isochrone parameters are physically inconsistent with both dwarf galaxies and globular clusters. We conclude that Indus II is likely a false-positive, flagged due to a chance alignment of stars along the line of sight.

Keywords: galaxies: dwarf — galaxies: fundamental parameters — methods: data analysis — methods: statistical — techniques: photometric

1. INTRODUCTION

With the advent of high-precision, large-area surveys such as SDSS (York et al. 2000), the Dark Energy Survey (DES; The Dark Energy Survey Collaboration 2005), Pan-STARRS (Chambers et al. 2016), the Hyper Suprime-Cam Subaru Strategic Program (HSC SSP; Homma et al. 2016), MagLites (Drlica-Wagner et al. 2016; Torrealba et al. 2018), and DELVE (Mau et al. 2019), the number of known faint satellite systems that orbit the Milky Way (MW) has dramatically increased (Drlica-Wagner et al. 2015; Koposov et al. 2015; Bechtol et al. 2015). The ambiguity of what constitutes a galaxy increases as more

systems are discovered that lie between the traditional loci of globular clusters and galaxies. Additionally, these low-luminosity systems challenge spectroscopic studies due to their low number of bright member stars (Willman & Strader 2012).

Many of these satellites discovered in the past decade are categorized as ultra-faint dwarf (UFD) galaxies (Simon 2019a). With $M_V \gtrsim -8$ mag ($M_* \lesssim 10^5 M_\odot$; Martin et al. 2008; Bullock & Boylan-Kolchin 2017), UFDs overlap with bright globular clusters (GCs) in the size-luminosity plane. Though they overlap in this parameter space, UFDs and GCs likely have different formation

mechanisms (Forbes et al. 2018). From their internal stellar kinematics, GCs are consistent with having little or no dark matter, and may be remnants of nucleated dwarf galaxies or may follow a completely separate evolutionary path (Bassino et al. 1994).

In contrast, the stellar kinematics of UFDs exhibit high M/L_V ratios (i.e., $M/L_V \sim 10^3$; Simon & Geha 2007) and represent the faintest end of the galaxy luminosity function. Dynamical mass measurements are one of the primary distinguishing characteristics between UFDs and GCs. In comparison to low-luminosity GCs, UFDs have larger sizes ($r_h \gtrsim 30$ pc), larger velocity dispersions ($\sigma \gtrsim 3$ km s $^{-1}$), and significant metallicity spreads ($\sigma_{[Fe/H]} \gtrsim 0.3$ dex), as shown in Simon & Geha (2007) and Martin et al. (2007).

As the most dark matter dominated objects visible in the Universe, UFDs provide crucial, empirical information about the nature of dark matter and hierarchical structure at the smallest-scales (Frenk & White 2012; Bullock & Boylan-Kolchin 2017). In Λ -cold dark matter (Λ CDM) cosmology, structure forms hierarchically, with the UFDs corresponding to the galaxies in the smallest of dark matter halos (Wheeler et al. 2015; Sawala et al. 2015; Wetzel et al. 2016). Discerning the exact nature of MW satellites is therefore our paramount observational method to better constrain and compare cosmological models to low-luminosity systems. Firmly establishing the newly-discovered satellites as UFDs, and measuring their mass-to-light ratios, requires spectroscopic studies of a significant sample of their stars (e.g., Li et al. 2018).

However, due to the faintness of these systems, spectroscopy is only possible for a small sample of their stars, making a robust determination of their mass-to-light ratios difficult to obtain. In addition to spectroscopic studies, information on the structural parameters and stellar populations of UFDs may be obtained through deep photometric studies. For faint overdensities of stars like UFDs, this requires targeted imaging and precise photometry, in order to distinguish members of the systems from background stars and galaxies (e.g., Martin et al. 2008; Muñoz et al. 2012; Brown et al. 2014; Conn et al. 2018a,b; Jerjen et al. 2018; Mutlu-Pakdil et al. 2018).

In this work we seek to clarify the nature of two objects detected in the DES footprint, Grus I and Indus II, with deep Magellan/Megacam imaging.

Grus I was discovered by Koposov et al. (2015), however its status as a GC or UFD has not yet been totally disentangled due to its faintness ($M_V = -3.4$) and the lack of deep, wide field photometry. Follow-up studies based on the deep but small Gemini/GMOS-S field of view (FOV) photometry (Jerjen et al. 2018) were not

able to determine the properties of Grus I because of its extension ($r_h = 1'.77$, Koposov et al. 2015).

Martínez-Vázquez et al. (2019) obtained a precise distance to Grus I of $D_\odot = 127 \pm 6$ kpc ($\mu_0 = 20.51 \pm 0.10$ mag) from the detection of two RR Lyrae members. They find that this distance would imply a change of 5% in its previously calculated physical size, consistent with the estimate of Koposov et al. (2015). Given the large uncertainties in the previous determinations of physical size, deep and extended imaging in Grus I is needed to firmly confirm this.

Complementary spectroscopic studies made of this system (Walker et al. 2016; Ji et al. 2019) were not able to decipher the nature of this object either, since the velocity dispersion could not be resolved because of the scarce sample of members detected.

Our second target, DES J2038–4609, was identified in Drlica-Wagner et al. (2015) as a low-confidence UFD candidate and will be referred to as Indus II throughout the paper for convenience. The initial data for Indus II were located in a survey region with atypical non-uniformity as they were taken part-way through the survey observations. The primary evidence for candidacy stems from a clump of apparent blue horizontal branch (BHB) stars at $g \sim 22$. While Indus II has been targeted in some dark matter indirect detection analyses (Albert et al. 2017), there are no other studies confirming the nature of the object. Given the uncertainty associated with this system, we chose to confirm whether this target was a gravitationally bound system due to Magellan/Megacam’s FOV potentially covering $3 \times r_h$ (Drlica-Wagner et al. 2015).

We follow similar methods to other studies that have confirmed the status of many MW satellites as dwarf galaxies (see, e.g., Sand et al. 2012; Crnojević et al. 2016; Kim et al. 2016; Luque et al. 2016; Carlin et al. 2017; Conn et al. 2018a,b; Luque et al. 2018; Mutlu-Pakdil 2018). Our data complements other studies by utilizing a larger FOV (necessary for the potentially larger extents), while still resolving magnitudes ~ 3 magnitudes deeper than the discovery papers.

This paper is structured as follows. In §2 we describe the Magellan/Megacam and DES observations, photometry, and catalog selection. We present the likelihood method used to infer structural parameters in §3. In §4 we report the results from the statistical analysis, and §5 compares our results to previous results and concludes this work.

2. OBSERVATIONS AND DATA REDUCTION

2.1. Data

We observed Indus II and Grus I over four nights in April 2017 with the Megacam instrument (McLeod

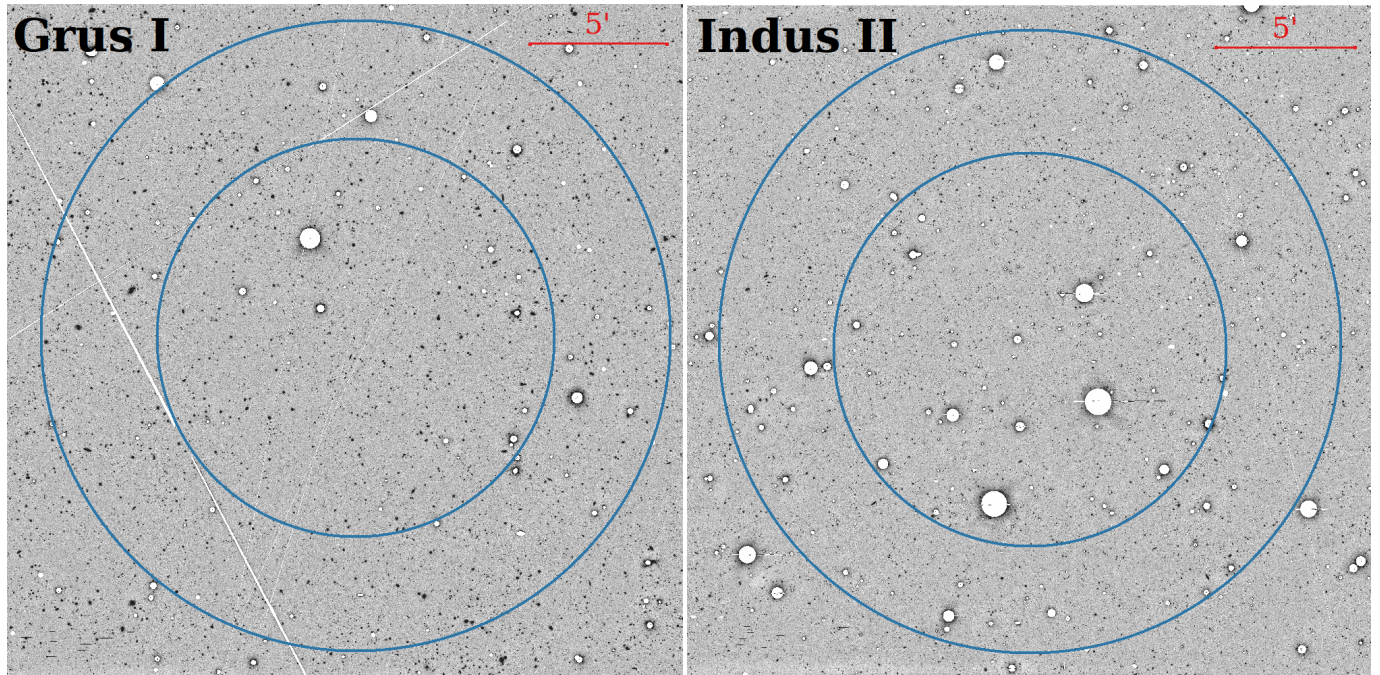


Figure 1. Full $24' \times 24'$ FOV of Grus I (left panel) and Indus II (right panel). Shown here are the final SWarped and coadded r -band images with masks applied to saturated objects and satellite trails (white marks). The inner blue circles delineate the region of interest (ROI; see §3) defined in the statistical analysis used to determine final properties of each object. The outer circles mark the outer limit of the area designated as the background region in the statistical analysis. For both objects, the radii of the circles are $r_{inner} = 7'$ and $7' \geq r_{background} \geq 12'$.

et al. 2015) at the $f/5$ focus of the 6.5 m Magellan Clay telescope. Megacam is an imager composed of 36 CCDs of 2048×4608 pixels, creating a square array with a FOV of $\sim 24' \times 24'$ (see Figure 1). The data were binned 2×2 resulting in a pixel scale of $0''.16$. Observations were dithered such that each image is offset by $+5''$ in right ascension (RA) and $+13''$ in declination (Dec.) from the previous one. This reduces the impact of the small gaps between the CCDs.

The data were reduced using the Megacam pipeline developed at the Harvard-Smithsonian Center for Astrophysics¹ (McLeod et al. 2006). This pipeline includes tasks such as bias subtraction, flat fielding, and cosmic ray correction. In addition, the pipeline derives astrometric solutions using the 2MASS survey (Skrutskie et al. 2006). The images were then resampled, with a lanczos3 interpolation function, and combined with a weighted average using SWarp (Bertin 2010). This process produced a final, stacked g - and r -band image for each object. An observing log can be found in Table 1.

2.2. Megacam Photometry

¹ This paper uses data products produced by the OIR Telescope Data Center, supported by the Smithsonian Astrophysical Observatory.

Table 1. Observing log of Magellan/Megacam observations in the g - and r -bands for Grus I and Indus II.

Object	UT Date	Filter	$N \times t_{exp}$ (s)	Seeing ($''$)
Gru I	2017 Apr 23	g	7×300	0.7
	2017 Apr 24	r	8×300	0.9
Indus II	2017 Apr 21	g	8×300	0.6
	2017 Apr 22	r	8×300	0.5

Due to the large FOV and number of objects in each image, we used point-spread function (PSF) fitting software to extract the stellar photometry. We used the well-known photometry package, DAOPHOT/ALLSTAR and ALLFRAME, and followed the general guidelines as described in various other papers to determine instrumental magnitudes (Stetson 1987, 1994).

An accurate PSF model was created from the brightest and most isolated unsaturated stars in the image. An initial coordinate list and aperture photometry pass of each image was done to find appropriate stars to be used in creating the PSF models. We chose 500 of the brightest stars, evenly distributed over the image, and visually inspected the surrounding areas and radial profiles for

Table 2. The photometric transformations between Megacam instrumental magnitudes and the DES photometric system. The fifth column displays the difference between the transformed Megacam magnitudes and the DES magnitudes. The sixth (sharp range) and seventh (median chi-value) columns detail the morphological cuts made on the instrumental photometry. The last two columns detail the number of stars and magnitude range of the final Megacam+DES stellar catalogs after these cuts were applied.

Object	Filter	β	α	std(Δ_{mag}) ^a	Sharp	Chi	# of stars	Magnitude range ^b
Grus I	<i>g</i>	7.554	-0.136	0.036	(-0.7, 1.2)	1.65	6743	(15.6, 26.7)
	<i>r</i>	7.651	-0.027	0.023	(-0.5, 0.7)	1.25	6743	(15.2, 26.3)
Indus II	<i>g</i>	7.596	-0.167	0.028	(-0.5, 0.3)	2.05	5520	(15.2, 26.6)
	<i>r</i>	7.657	-0.029	0.021	(-0.7, 0.2)	4.91	5520	(14.8, 26.8)

^aThe median absolute standard deviation of the difference between DES magnitudes and transformed Megacam magnitudes.

^bThe faint magnitude limits correspond to $S/N \sim 5$

saturation, neighbors, bad pixels, and other effects that might affect the measurement of an object. In order to represent stars over the entire FOV, we ensured that the remaining stars were distributed over the entire image and allowed the PSF to vary quadratically. It should be noted that due to the elongation of objects in the Grus I *g*-band image, the fitting radius was set to be slightly larger than the FWHM to better encompass the core of the star. The elongation is along the East-West axis and likely due to tracking issues.

In order to create a final coordinate list, ALLSTAR was used twice to perform preliminary PSF photometry on the images. The first run produced a star-subtracted image on which ALLSTAR was run the second time and the stars used in the psf-fit and neighbors were visually inspected. This allows for the detection of fainter objects, located in the PSF wings of brighter objects. The resultant object list is then input to ALLFRAME to perform a final round of PSF photometry on each filter simultaneously. In order to convert pixel coordinates from one filter to another, DAOMATCH/DAOMASTER is used to find a linear transformation between the *g*- and *r*-bands for each image. This last step creates a final catalog in each filter that is matched by object ID. It also mitigates the systematic uncertainty created by blended stars being inaccurately measured as one star in some frames.

2.3. DES Photometry

We used DES photometry to transform Megacam instrumental magnitudes to DES standard magnitudes and to find magnitudes for the stars saturated in Megacam. DES is a wide-field survey imaging 5000 deg² of the southern hemisphere (The Dark Energy Survey Collaboration 2005; Dark Energy Survey Collaboration et al. 2016). DES uses the Dark Energy Camera (DECam; Flaugher et al. 2015) positioned at the prime focus of the 4-meter

Blanco telescope at the Cerro Tololo Inter-American Observatory (CTIO) in Chile. DES data are reduced by the DES Data Management (DESDM) pipeline; in which they are detrended, astrometrically calibrated to 2MASS, and coadded into image tiles (?). Detrending includes standard bias subtraction, CCD cross talk, flat fielding, and non-linearity, pupil, fringe, and illumination corrections. Object detection, photometric, and morphological measurements were performed with SExtractor followed by multi-epoch and single-object fitting (SOF; Abbott et al. 2018).

The DES catalogs used in this work were created from the DES Y3 GOLD (v2.0) catalog with the selection flags `FLAGS_GOLD=0` and `EXTENDED_CLASS_MASH_SOF≤2` in order to ensure we have a complete stellar sample with minimal contaminants. The `FLAGS_GOLD` selection applies a bitmask for objects that have known photometric issues and artifacts. The `EXTENDED_CLASS_MASH_SOF` is similar to the extended classification variables defined in Equations 1, 2, and 3 in Shipp et al. (2018), but for the SOF photometry. The variables in these equations classify objects as high-confidence stars, low-confidence stars, and low-confidence galaxies.

2.4. Transformation from Megacam to DES

The matched objects found in the previous section were used to find a transformation between DES magnitudes and Megacam instrumental magnitudes. A color cut of $(g_0 - r_0)_{DES} < 1.2$ was applied to remove a clump of M0 and redder stars. We used only stars having DES photometric errors less than 0.03 mag. These criteria ensure that a high-quality stellar sample is utilized in finding the magnitude system transformation.

To perform this transformation, we solve for the coefficients of the following equation using a generalized least

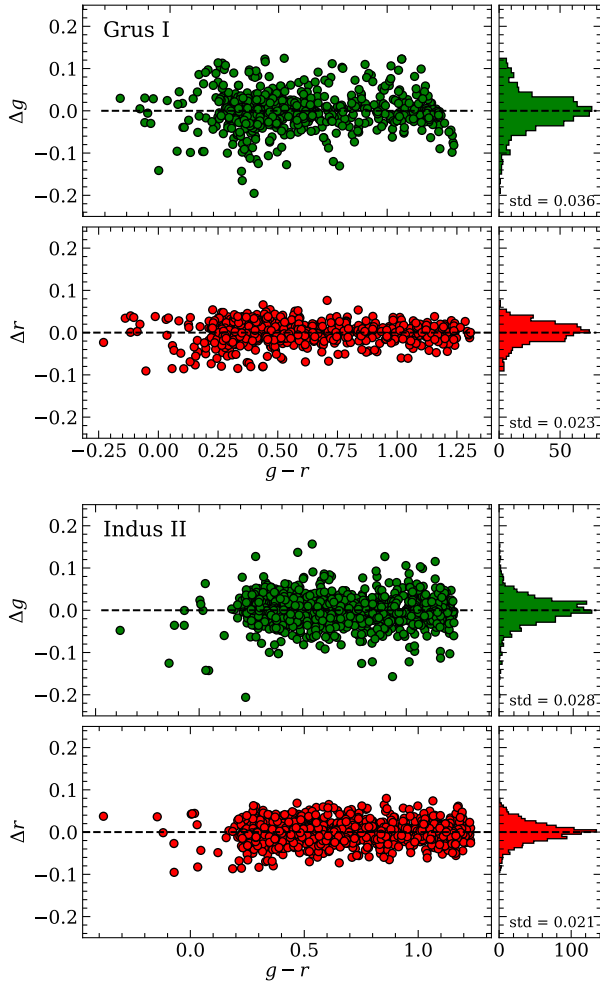


Figure 2. Distribution of high confidence stars used in photometric transformation from Megacam instrumental magnitudes to the DES magnitude system. All four panels show $m_{DES} - m_{Megacam}$ vs. $g - r$ (Megacam), where Megacam here are transformed into the DES system. The top two panels show Grus I (586 matched stars) and the bottom two panels show Indus II (1122 matched stars). For both objects, the green points represent g -band data and the red points represent r -band data.

squares regression:

$$M_{DES} = m_{instr} + \beta + \alpha(g_0 - r_0)_{DES}, \quad (1)$$

where β is the zeropoint offset and α is the color coefficient. To find the true distribution of $M_{DES} - m_{instr}$, we run the catalog through a sigma-clipping algorithm based on the median absolute deviation. Stars that lie outside 3σ are clipped until the distribution converges. Equation 1 is then applied to all of the instrumental magnitudes found from ALLFRAME. A second-order fit was explored and deemed unnecessary. The coefficients of this fit are in the third and fourth columns in Table 2 and the difference between transformed Megacam mag-

nitudes and DES magnitudes of stars used to find the transformation can be seen in Figure 2.

We created the final stellar catalog by applying morphological cuts using the statistics $sharp$ and χ which were determined during the PSF fitting. $Sharp$ can be approximated as $sharp^2 \sim \sigma_{obs}^2 - \sigma_{PSF}^2$, where σ_{obs} is the observed photometric error and σ_{PSF} is the expected photometric error (Stetson 1987).

The second statistic, χ , is the ratio of observed pixel-to-pixel scatter over expected scatter, determined from the intrinsic scatter in the PSF models. Star galaxy separation begins to break down at fainter magnitudes, i.e., $g_0 \sim 25.5$ and $r_0 \sim 24.75$. The details of these cuts and the magnitude range of the final stellar catalogs can be found in the last four columns in Table 2. In addition, the final catalog’s brighter magnitudes are supplemented by the DES stellar objects where Megacam saturates at $g_0 \sim 18$ and $r_0 \sim 17.5$. A portion of these catalogs can be seen in Tables 3 and 4.

Figure 3 shows the color-magnitude diagrams (CMDs) created for both Grus I and Indus II using the final calibrated stellar catalog as it was described in this section. The uncertainties show that the photometric signal-to-noise ~ 10 to a depth ~ 3 magnitudes below that of the discovery papers.

Table 3. The final calibrated stellar catalog for Grus I—Sorted by star ID. This table is published in its entirety in machine-readable format. A portion is shown here for guidance regarding its form and content. All magnitudes are in the DES magnitude system.

Star ID	R.A.	Dec.	$g_{0,DES}$ (mag)	σ_g (mag)	$r_{0,DES}$ (mag)	σ_r (mag)
12543	344.134	-50.285	25.398	0.106	24.807	0.068
12845	344.139	-50.284	22.623	0.007	22.402	0.007
13343	344.138	-50.281	24.075	0.029	24.044	0.036
14597	344.103	-50.278	24.745	0.047	24.361	0.049
14730	344.168	-50.278	24.956	0.070	24.902	0.076
15406	344.187	-50.275	17.679	0.003	17.276	0.002

3. METHODS

We utilize the Ultra-faint Galaxy Likelihood (UGaLi)² toolkit to determine structural parameters and the best-fitting isochrones for Grus I and Indus II. Here we review the aspects of UGaLi that are important for our analysis, and refer to Bechtol et al. (2015) and the appendix of

² <https://github.com/DarkEnergySurvey/ugali>

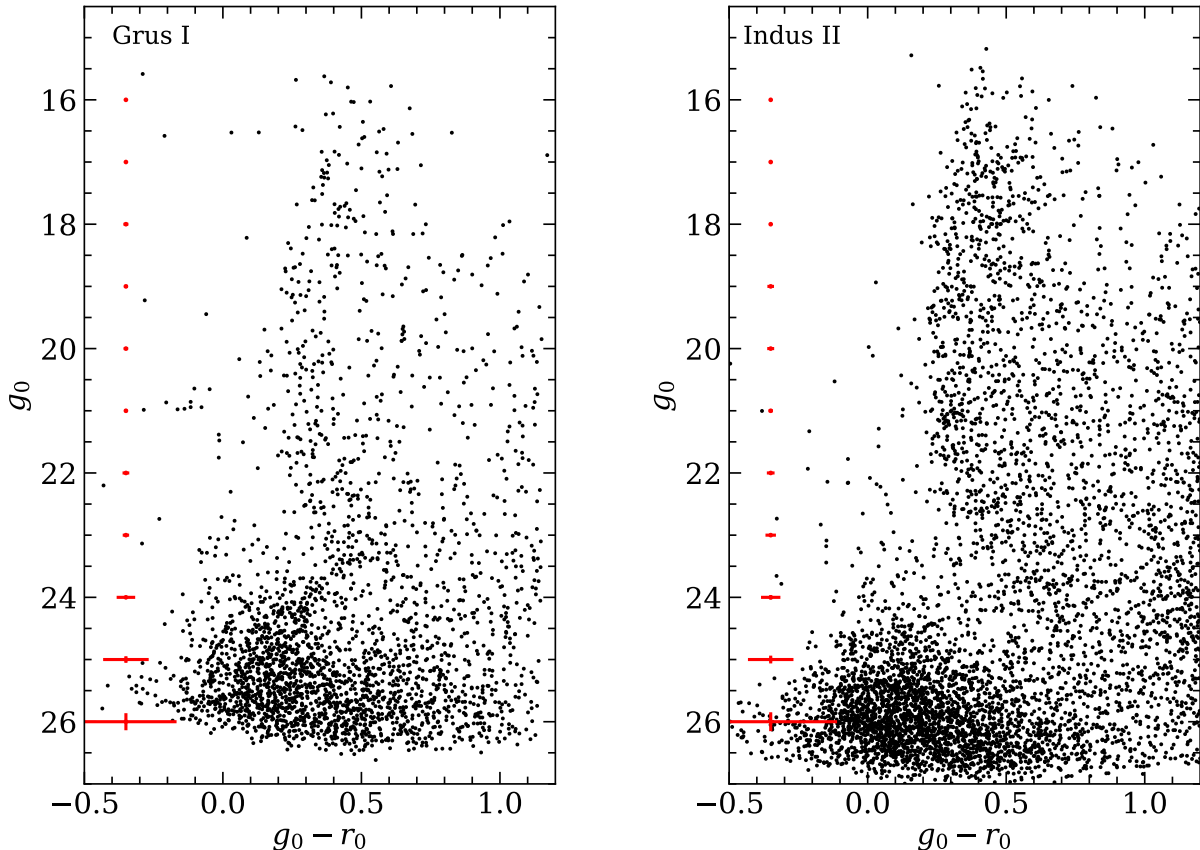


Figure 3. g_0 vs. $(g_0 - r_0)$ CMDs of the full $24' \times 24'$ Megacam FOV centered on Grus I (left) and Indus II (right)—created with the final stellar Magellan/Megacam+DES catalog (where objects $g_0 \lesssim 18$ and $r_0 \lesssim 17.5$ are from DES). The error bars represent median photometric uncertainties for one-mag wide bins and are arbitrarily placed in color-space.

Table 4. The final calibrated stellar catalog for Indus II—Sorted by star ID. This table is published in its entirety in machine-readable format. A portion is shown here for guidance regarding its form and content.

Star ID	R.A.	Dec.	$g_{0,DES}$ (mag)	σ_g (mag)	$r_{0,DES}$ (mag)	σ_r (mag)
17138	309.735	-46.284	25.845	0.125	25.532	0.090
17539	309.705	-46.283	25.911	0.117	25.658	0.100
17819	309.691	-46.282	21.532	0.007	20.891	0.006
18608	309.677	-46.278	21.129	0.005	20.183	0.010
18821	309.764	-46.278	25.005	0.064	24.897	0.052
19208	309.689	-46.276	21.143	0.006	20.198	0.010

Drlica-Wagner et al. (2019) for a more detailed description.

Our data sample consists of the magnitude and the error on the magnitude in two filters, $\mathcal{D}_{c,i} = \{g_i, \sigma_{g_i}, r_i, \sigma_{r_i}\}$, and the spatial positions of the stars $\mathcal{D}_{s,i} = \{\alpha_i, \delta_i\}$. We define the probability distribution

for the structural parameters as u_s , and the probability distribution for the parameters of the isochrone as u_c . The total probability distribution function (PDF) for the data $\mathcal{D}_i = \{\mathcal{D}_{s,i}, \mathcal{D}_{c,i}\}$ given the model parameters θ is then

$$u(\mathcal{D}_i|\theta) = u_s(\mathcal{D}_{s,i}|\theta_s) \times u_c(\mathcal{D}_{c,i}|\theta_c), \quad (2)$$

This probability distribution is defined such that the integral of it over the entire spatial and magnitude domain is unity.

For the structural properties, u_s , we assume an elliptical Plummer model, with a projected density distribution (Plummer 1911; Martin et al. 2008),

$$\Sigma(R) \propto \left[1 + \left(\frac{R_i}{R_p} \right)^2 \right]^{-2}. \quad (3)$$

Here R_i is the elliptical radius coordinate from the center of the galaxy, and R_p is the Plummer-scale radius (equivalent to the 2D azimuthally averaged half-light radius, $r_h = a_h \sqrt{1 - \epsilon}$). There are five model parameters that describe the Plummer profile: the centroid coordinates (α_0, δ_0) , the semi-major half-light radius (a_h),

the ellipticity (ϵ), and position angle (ϕ). The density distribution is further related to spatial position by

$$R_i = \left\{ \left[\frac{1}{1-\epsilon} (X_i \cos \phi - Y_i \sin \phi) \right]^2 - (X_i \sin \phi + Y_i \cos \phi)^2 \right\}^{\frac{1}{2}} \quad (4)$$

and spatial position is related to the object centroid by

$$X_i - X_0 = (\alpha_i - \alpha_0) \cos(\delta_0) \quad (5)$$

and

$$Y_i - Y_0 = \delta_i - \delta_0. \quad (6)$$

For the isochrone properties, u_c , we calculate the PDF by binning the color-magnitude information over a grid of isochrones that are weighted by a Chabrier IMF (Chabrier 2003) and have a fixed solar alpha abundance. These isochrones are described in terms of the distance modulus ($m - M$), the age of the stellar population (τ), and the metallicity (Z). All metallicities are reported as $[\text{Fe}/\text{H}] = \log_{10} \left(\frac{Z}{Z_\odot} \right)$, with $Z_\odot = 0.0152$.

The grid of PARSEC isochrones are representative of old metal-poor stellar populations, i.e., $0.0001 < Z < 0.001$, $1 \text{ Gyr} < \tau < 13.5 \text{ Gyr}$, and $16.0 < m - M < 25.0$ to fit the CMD properties of each object (Bressan et al. 2012). We check that our results do not depend on the isochrone model by comparing to Dotter (2016) and find that they are insensitive to this specific assumption.

With the above model, we can define the Poisson log-likelihood

$$\log \mathcal{L} = -\lambda N_s - \sum_i^{\text{stars}} \log(1 - p_i), \quad (7)$$

where λ , the stellar richness, is a normalization parameter representative of the total number of member stars with $M_* > 0.1M_\odot$ in the satellite, N_s is the fraction of observable satellite member stars, and p_i is the probability that a star is a member of the satellite.

Because we choose to normalize the signal PDF to unity, we can interpret λ as the total number of stars in the satellite (observed + unobserved). The membership probability is given by

$$p_i = \frac{\lambda u_i}{\lambda u_i + b_i}, \quad (8)$$

where b_i is the background density function (for more details see Appendix C in Drlica-Wagner et al. 2020). We take the background density function to be independent of spatial position in our region of interest (ROI).

The empirical background density function, b_i , is determined from an annulus ($7.2 < r < 12'$) surrounding our target ROI ($r < 7.2$). We require the ROI to be $\gtrsim 2 \times r_h$. This is the maximum ROI that still allows for the background annulus to contain $\sim 3 \times r_h$ (Martin et al. 2008), where r_h is from Koposov et al. (2015); Drlica-Wagner et al. (2015). Figure 1 depicts these regions as blue circles. Any non-stellar objects that still contaminate the data at greater magnitudes are expected to do so equally over the entire FOV and therefore averaged within b_i .

With λ allowed to vary and b_i held fixed, we simultaneously explore the whole parameter space with flat priors for all parameters except r_h (an inverse prior). With UGaLi, we run an MCMC chain with 100 walkers, 12000 steps, and 1000 burn-in (Foreman-Mackey et al. 2013). Absolute V -band magnitude is determined following the prescription of Martin et al. (2008)

4. RESULTS & DISCUSSION

4.1. Grus I

Column 1 of Table 5 lists the parameters obtained from the median peak likelihood of the posterior distributions (see Figure 4). With our improved parameters for Grus I, we find it to be consistent with an extended ultra-faint dwarf galaxy that resides at the faint edge ($\mu \sim 30$ mag) of the galaxy locus in the size-luminosity plane. Figure 5 shows the relationship between GCs and UFDs in this parameter space and also shows the updated location of Grus I. Table 5 lists the parameters that were derived in previous works (both Grus I and Indus II are represented).

With a $a_h \sim 202$ pc and $M_V \sim -4.1$, Grus I is both larger and brighter than estimates from previous works (Koposov et al. 2015). In addition, according to our results ($[\text{Fe}/\text{H}] \sim -1.9$), it is among the more metal-rich UFDs found to date (Simon 2019b). Spectroscopic studies by Walker et al. (2016); Ji et al. (2019) find the brightest potential member stars are very metal poor (e.g., $[\text{Fe}/\text{H}] \sim -2.3$), whereas photometric studies (including this one) find it to be less metal poor, i.e., $[\text{Fe}/\text{H}] \lesssim -2$ (Koposov et al. 2015; Jerjen et al. 2018). A larger spectroscopic sample is required to confirm the metallicity of this object.

This discrepancy between spectroscopic and photometric metallicities has been seen in previous studies (see Section 4.3 in Caldwell et al. 2017). In that case, it was considered more likely that the spectroscopic results were likely systematically metal-poor. There was very good agreement with the isochrone calculated with the photometric metallicity and probable member stars.

Figure 6 shows the CMD of the stars within $2 \times r_h$ and the CMD of the background (see the 1st and 2nd

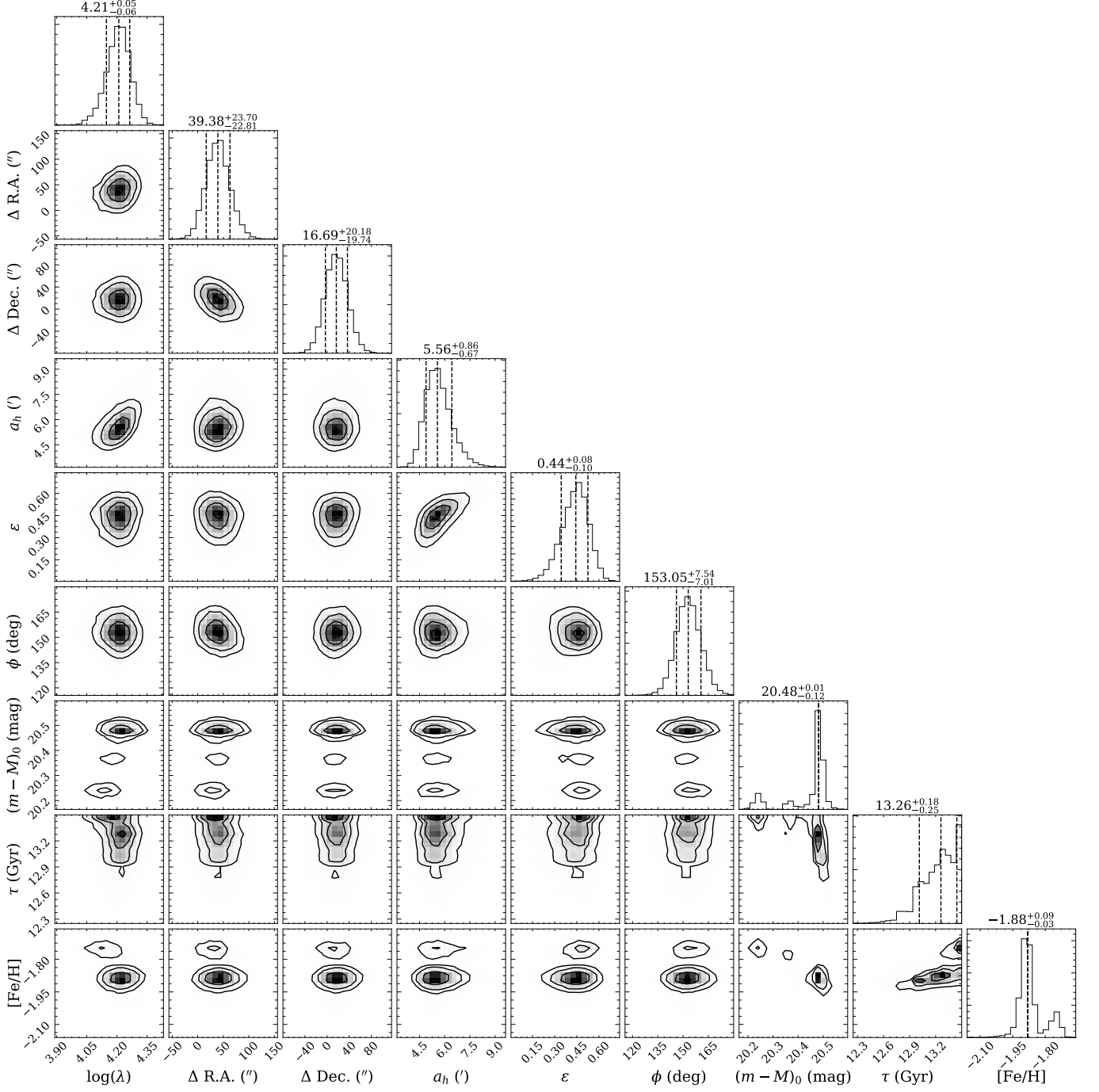


Figure 4. Posterior probability distributions for the structural and isochrone parameters of Grus I obtained from an elliptical Plummer model and grid of PARSEC isochrones. The parameters explored were (from left to right): stellar richness (λ), Δ R.A. & Δ Dec. (these are the shift from the centroid found in [Koposov et al. \(2015\)](#)), semi-major half-light radius (a_h), ellipticity (ϵ), position angle (ϕ), distance modulus ($(m - M)_0$), age (τ), and metallicity ($[\text{Fe}/\text{H}]$). Dashed lines in the 1D histograms indicate 16th, 50th, and 84th quantiles of the median peak likelihood. We have excluded these quantiles from $(m - M)_0$ and $[\text{Fe}/\text{H}]$ due to their bimodality.

Table 5. Photometric and spectroscopic parameters of Grus I and Indus II found in the literature prior to this work. The columns for Grus I, in order, are from this work, [Koposov et al. \(2015\)](#); [Walker et al. \(2016\)](#); [Jerjen et al. \(2018\)](#); [Muñoz et al. \(2018\)](#); [Ji et al. \(2019\)](#); [Martínez-Vázquez et al. \(2019\)](#). Column 8 describes Indus II as found in the discovery paper, [Drlica-Wagner et al. \(2015\)](#).

	Grus I							Indus II
	This Work (1)	(2)	(3)	(4)	(5)	(6)	(7)	(8)
α_{2000} (deg)	$344.166^{+0.007}_{-0.006}$	344.1765	...	344.1700	344.1797	309.76
δ_{2000} (deg)	$-50.168^{+0.006}_{-0.005}$	-50.1633	...	-50.1641	-50.1800	-46.16
t-value (σ)	21.3	10.1	~ 5.7
M_V (mag)	-4.1 ± 0.3	-3.4 ± 0.3	-4.3 ± 0.19
D_{\odot} (kpc)	125^{+6}_{-12}	120	...	115 ± 6	214 ± 16
r_h (arcmin)	$4.16^{+0.54}_{-0.74}$	$1.77^{+0.85b}_{-0.39}$	0.81 ± 0.66^b	$2.9^{1.1b}_{1.0}$
r_h (pc)	151^{+21}_{-31}	$62^{+29.8}_{-13.6}$	28.3 ± 23.0	181 ± 67
ϵ	$0.44^{+0.08}_{-0.10}$	$0.41^{+0.20}_{-0.28}$	0.45 ± 0.30	< 0.4
ϕ (deg)	$153^{+8.0}_{-7.0}$	4 ± 60	23 ± 18
$m - M$ (mag)	$20.48^{+0.11a}_{-0.22}$	20.4	...	20.30 ± 0.11	20.51 ± 0.10^c	...
τ (Gyr)	$13.26^{+0.18}_{-0.25}$	$14.0^{+1.0}_{-1.0}$
$[Fe/H]$ (dex)	$-1.88^{+0.09}_{-0.03}$...	$-1.42^{+0.55}_{-0.42}$	$-2.5^{+0.3}_{-0.3}$	-2.5 ± 0.3	$-2.57, -2.50$
$\sigma_{[Fe/H]}$ (dex)	< 0.9
$\langle v_{LOS} \rangle$ (km s $^{-1}$)	$-140.5^{+2.4}_{-1.6}$
$\sigma_{v_{LOS}}$ (km s $^{-1}$)	< 9.8
$M_{\odot}/L_{V,\odot}$	< 2645

^aA systematic uncertainty of 0.1 mag was added to account for the difference between best-fits for [Bressan et al. \(2012\)](#) and [Dotter \(2016\)](#) isochrones.

^bSemi-major halfflight radii converted from azimuthally-averaged radii with $\sqrt{1 - \epsilon}$ factor.

^cThis distance measurement is based on two RR Lyrae stars found in Grus I.

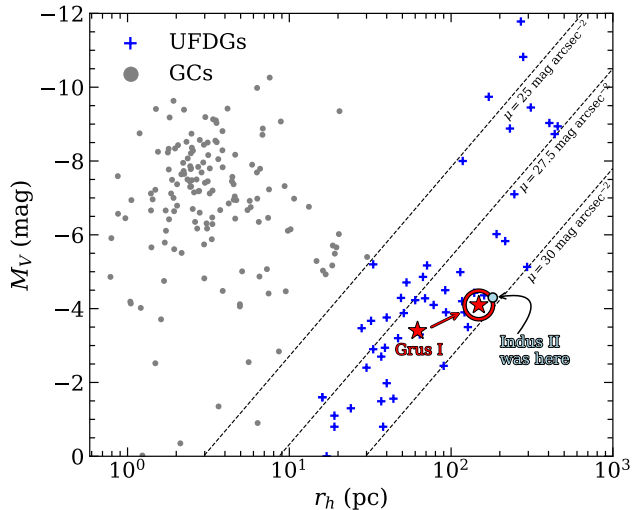


Figure 5. Shown as a red star are the position of Grus I with our newly derived properties (circled in red) and its original location in the size-luminosity plane. The original location of Indus II is shown as a light blue circle. The MW globular clusters are in grey points and the rest of the MW UFDs are depicted with blue crosses.

panel, respectively). The last three panels of Figure 6 are Hess diagrams of the background stellar density, the stellar density within $2 \times r_h$, and the difference of the two (see panels 3, 4, and 5, respectively). Overlaid in the 1st, 4th, and 5th panels is a PARSEC isochrone representative of an old, metal-poor population with $\tau = 13.3$ Gyr and $[\text{Fe}/\text{H}] = -1.9$. This isochrone agrees with the best-fit properties of Grus I inferred from the maximum likelihood distribution.

For Grus I the background-subtracted Hess diagram shown in the 5th panel of Figure 6, clearly illuminates MSTO, MS, and sub-giant branch features that are well-represented by the inferred properties. Less obvious, but still well-populated, the isochrone clearly delineates a HB and RGB population. It should be noted that some potential members can still be seen in the second top-row panel (background CMD) of Figure 6 due to Grus I’s large extent.

In the left two panels of Figure 7, we show the distribution of the UGaLi membership probabilities in sky coordinates and color-magnitude space. These membership probabilities were determined as described in §3. The three panels in this figure show that our inferred parameters describing the stellar population and morphology of Grus I are consistent with a theoretical Plummer profile.

These probabilities were further used to create a binned and weighted density profile as seen in the far right panel of Figure 7. There are an equal number of stars in each

bin. It can be seen that the binned data fits well over the Plummer model profile shown as the dashed line.

The posterior distributions and maximum-likelihood peak values are shown in Figure 4. While some of the properties shown in Figure 4 agree with previous works (see Table 5) within the uncertainties (e.g., centroid coordinates, ellipticity, distance modulus), others have shifted slightly in this work (i.e., r_h), changing some of the derived properties.

Jerjen et al. (2018) find two small overdensities at $[(\alpha - \alpha_0), (\delta - \delta_0)] \approx [+0.2, -0.5]$ (arcmin) and $[(\alpha - \alpha_0), (\delta - \delta_0)] \approx [-0.6, +0.8]$ (arcmin)—with extents of 22×25 pc and 13×28 pc, respectively. It is interesting to note that we do not find obvious evidence of the two slight overdensities or diffuse centroid found in Jerjen et al. (2018). Our centroid shift does not seem to be significant or dependent on any lack of dense central overdensity as can be seen in Figure 8. The dashed yellow line in this figure indicates the half-light radius created with our inferred parameters.

The r_h (4’16) found in this work is larger than previous works by more than a factor of 2. Our larger FOV (see Figure 1) allows us to more accurately constrain the local background contamination and is likely the reason for the change in extent. Additionally, we find Grus I to be about one magnitude brighter ($M_V \sim -4.1$ mag) than previously thought (Koposov et al. 2015), while the distance to the object is in agreement with the recently updated distance determination based on RR Lyrae stars (Martínez-Vázquez et al. 2019).

It should be noted that Jhelum, a nearby stellar stream ($D_\odot \sim 13$ kpc, $m - M \sim 15.6$; Shipp et al. 2018), potentially contaminates the FOV. In order to test this, we cut potential stream member stars from our catalog and performed the same analysis on the new catalog. These potential members were chosen based on Jhelum’s spatial footprint and location in color-magnitude space. The width of the area in color-magnitude space was chosen to account for our photometric uncertainties. The distance of the Jhelum stream ($D_\odot \sim 13$ kpc) compared to how far Grus I is precludes any physical association between the two. The results from this analysis were the similar within uncertainties. Therefore, we determined that the presence of the stream does not significantly affect our analysis.

4.2. Indus II

MCMC chains run on this object fail to converge and no membership probabilities are calculated. The resulting isochrone parameters from the uncovered chains are indicative of a young stellar population, which is inconsistent with UFDs or globular clusters.

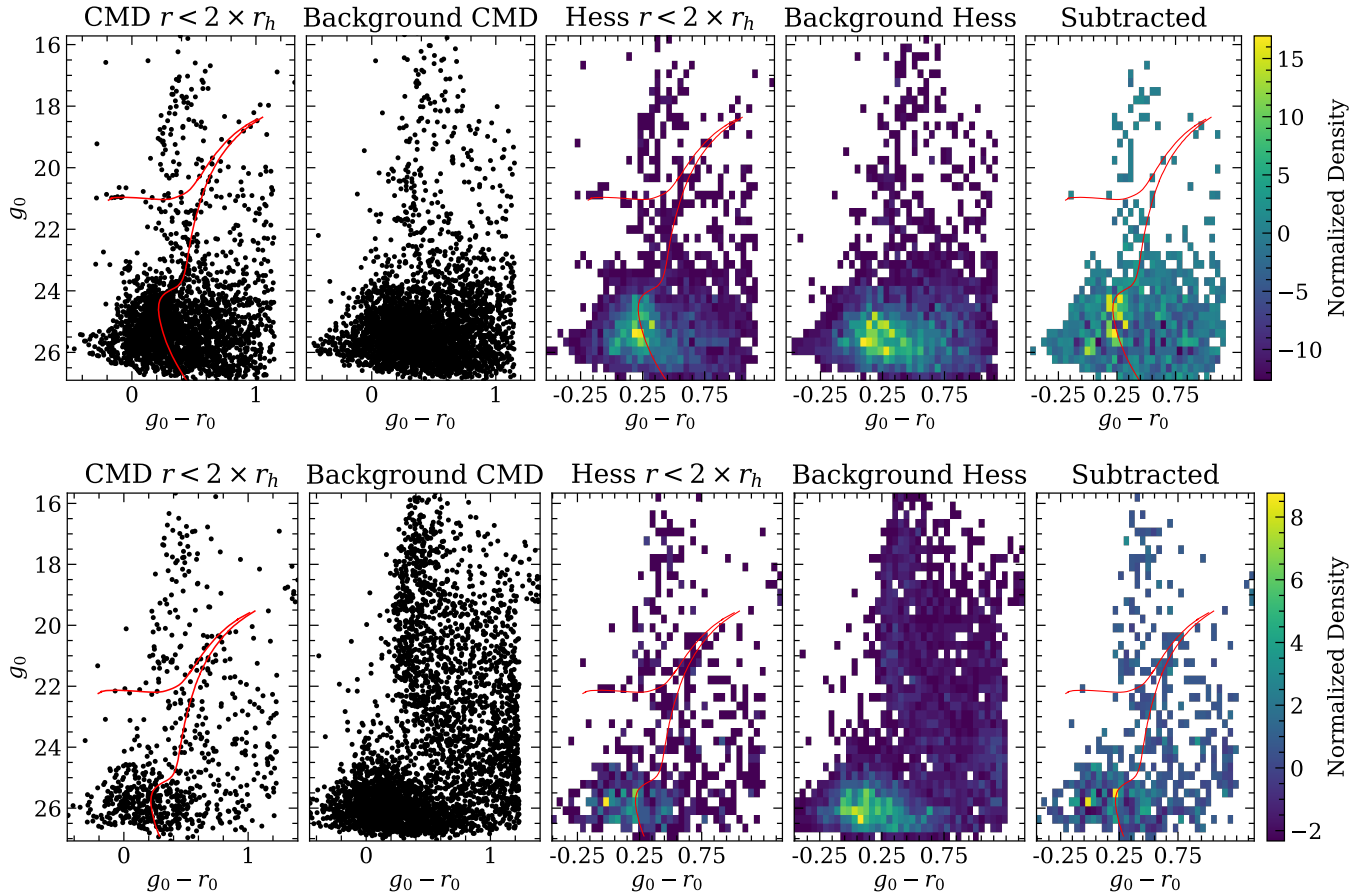


Figure 6. The top row of panels is for Grus I CMD and the bottom row is for Indus II CMD. In both cases, the 1st panel shows an ROI of $2 \times r_h$ centered on the object, where Grus I uses properties found in this study (see Table 5) and Indus II uses the discovery properties from [Drlica-Wagner et al. \(2015\)](#). The 2nd panel is a comparison CMD made from stars $> 2 \times r_h$ away from the ROI. The 3rd panel is a Hess diagram showing the density of the background stars seen in the 2nd panel. They have been scaled to match the same area as the ROIs. The 4th panel is the Hess diagram of the stars within $2 \times r_h$ as seen in the 1st panel. The 5th panel is the Hess difference of the 4th and 3rd panels.

In all but the background panels of Figure 6, the UFD representative old, metal-poor isochrone delineates the HB but fails to match with any other CMD feature. The derived isochrone fails to match the BHB stars that its candidacy hinged on originally. This indicates Indus II is likely a false-positive, i.e., neither a dwarf galaxy nor a globular cluster.

Since we have found that Indus II is neither a real galaxy nor a cluster, it goes against convention to use Indus II as its designation. We prefer to use the designation DES J2038–4609 from now on.

5. CONCLUSIONS AND FINAL REMARKS

We confirm the status of Grus I as a likely dwarf galaxy with the results of an MCMC algorithm and fit to a Plummer density model with deep Magellan/Megacam follow-up photometry of the objects Grus I and DES J2038–4609. This photometry reaches $\sim 2 - 3$ magni-

tudes deeper than the discovery data, allowing us to derive i) improved distance, which is in agreement with the distance obtained using RR Lyrae distance indicators ([Martínez-Vázquez et al. 2019](#)), ii) luminosity, 1 mag brighter than [Koposov et al. \(2015\)](#), and iii) structural parameters, particularly finding that the r_h is two times larger. We find that DES J2038–4609 is a false positive that was flagged due to a chance projection of an overdensity of stars.

Grus I is an extended ($r_h \approx 4'.16$), elliptical ($\epsilon = 0.44$) dwarf galaxy with a distance of 125 kpc. Like other dwarfs, Grus I has an old single, stellar population (13.3 Gyr) with low metallicity ($[\text{Fe}/\text{H}] = -1.9$). Its luminosity ($M_V \approx -4.1$) and azimuthal half-light radius (151 pc) place it at the lower edge of the dwarf locus in the size-luminosity plane (see Figure 5).

Our analysis complements previous studies with a larger FOV and deeper photometry, allowing us to con-

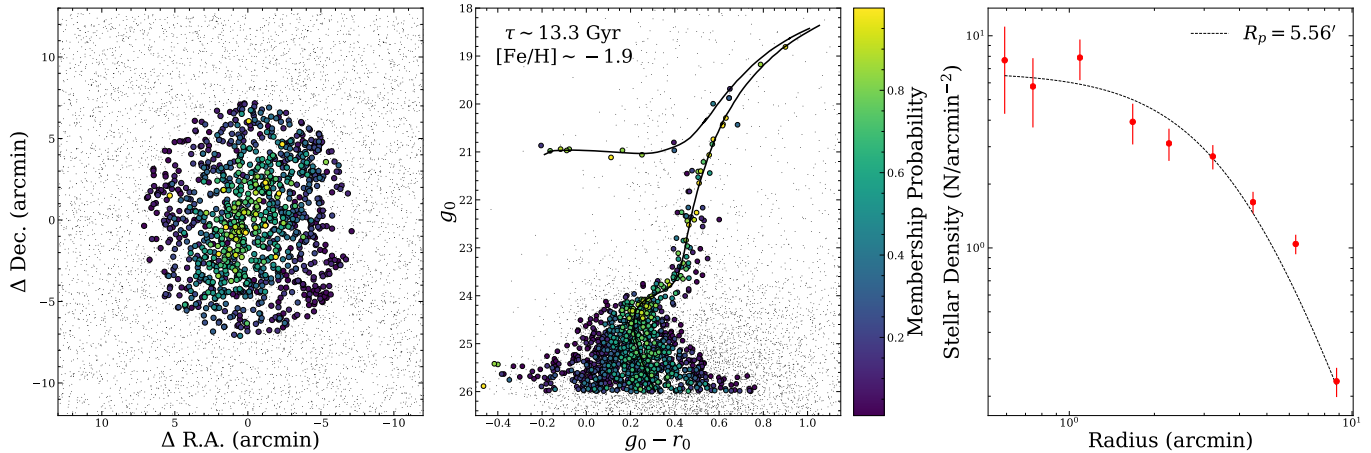


Figure 7. Right panel: Spatial distribution of stars in Grus I that have high membership probability. Middle Panel: Color-magnitude diagram of the same stars with high membership probability. The black line is the isochrone best described by our newly derived parameters in Table 5. Gray points in both panels are stars with less than 5% membership probability. Right panel: The stellar density profile of Grus I where the data is shown in red in elliptical bins of equal number and weighted by associated membership probabilities. The black dashed line shows the theoretical two-dimensional Plummer profile created with a Plummer-scale radius equal to $a_h = 5.6'$.

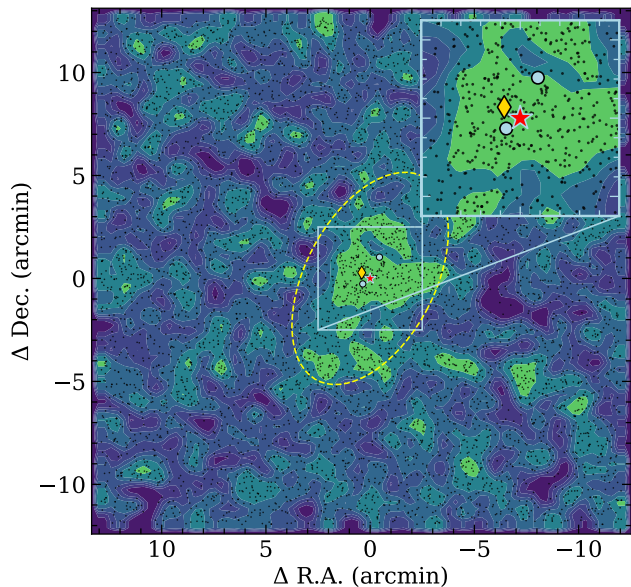


Figure 8. The $3 - \sigma$ iso-density contours of Grus I with our redetermined centroid shown as a red star. The blue circles represent the location of the two overdensities mentioned in Jerjen et al. (2018) and the gold diamond is the original centroid found in Kposov et al. (2015). The yellow dashed ellipse indicates the Plummer half-light radius found in this work.

firm the suggestion of Walker et al. (2016) that Grus I was likely larger in extent³. We also find that Grus I is slightly less metal-poor than most UFDs, with $[\text{Fe}/\text{H}] \lesssim -1.9$ al-

³ This larger extent implies a lower-density dark matter halo (Wolf et al. 2010)

though not as metal-rich as suggested in Walker et al. (2016).

In this work, we reach the necessary FOV ($24' \times 24'$) which allows us to improve upon and find new structural parameters of Grus I. Martin et al. (2008) determined that a FOV three times the half-light radius is necessary to accurately constrain the structural properties of UFDs. Therefore, with $r_h \sim 4'16'$, our $24' \times 24'$ FOV is just large enough to derive accurate structural parameters.

Previous spectroscopic studies find mixed results with respect to the average metallicity of this object. There are two well-measured, brighter member stars that are consistent with old, metal-poor UFDs ($[\text{Fe}/\text{H}] \sim -2.5$), but Walker et al. (2016) found five faint stars that suggested a metallicity of $[\text{Fe}/\text{H}] \sim -1.4$. It is possible that these fainter stars have a systematic uncertainty or bias that cause Grus I to appear more metal-rich than it is.

We analyze DES J2038–4609 with background subtracted Hess diagrams and UGalLi and find that the distribution of stars does not correlate with any isochrone or Plummer model. A chance alignment of possible BHB stars contributed to the original detection of DES J2038–4609 as a candidate satellite. Constraining power for this overdensity comes from a set of BHB stars. This feature can be seen in our dataset as well, but does not match a corresponding MSTO that is consistent with a UFD. We conclude that DES J2038–4609 is not consistent with either a dwarf galaxy or a globular cluster.

Ongoing follow-up studies of UFDs will continue to have important implications for our understanding of near-field cosmology. As the most dark matter dominated objects and the only resolved examples of these

old, relatively pristine stellar populations, it is important that their nature is well understood. Understanding their nature contributes to the characterization of the satellite population of the MW, leading to more accurate inferences about galaxy formation physics and the nature of dark matter. Studies with deep and wide follow-up photometry, such as this one, are useful to help characterize these faint objects.

ACKNOWLEDGEMENTS

This paper has gone through internal review by the DES collaboration. The authors thank Taylor A. Hutchison, Jonathan H. Cohn, and Peter S. Ferguson for their insightful conversation and support throughout this analysis. SAC acknowledges support from the Texas A&M University and the George P. and Cynthia Woods Institute for Fundamental Physics and Astronomy. ABP acknowledges support from NSF grant AST-1813881. JDS acknowledges support from NSF grant AST-1412792. This research made use of Astropy,⁴ a community-developed core Python package for Astronomy ([Astropy Collaboration et al. 2013, 2018](#)). This research made extensive use of [arXiv.org](#) and NASA’s Astrophysics Data System for bibliographic information.

Funding for the DES Projects has been provided by the U.S. Department of Energy, the U.S. National Science Foundation, the Ministry of Science and Education of Spain, the Science and Technology Facilities Council of the United Kingdom, the Higher Education Funding Council for England, the National Center for Supercomputing Applications at the University of Illinois at Urbana-Champaign, the Kavli Institute of Cosmological Physics at the University of Chicago, the Center for Cosmology and Astro-Particle Physics at the Ohio State University, the Mitchell Institute for Fundamental Physics and Astronomy at Texas A&M University, Financiadora de Estudos e Projetos, Fundação Carlos Chagas Filho de Amparo à Pesquisa do Estado do Rio de Janeiro, Conselho Nacional de Desenvolvimento Científico e Tecnológico and the Ministério da Ciência, Tecnologia e Inovação, the Deutsche Forschungsgemeinschaft and the Collaborating Institutions in the Dark Energy Survey.

The Collaborating Institutions are Argonne National Laboratory, the University of California at Santa Cruz,

the University of Cambridge, Centro de Investigaciones Energéticas, Medioambientales y Tecnológicas-Madrid, the University of Chicago, University College London, the DES-Brazil Consortium, the University of Edinburgh, the Eidgenössische Technische Hochschule (ETH) Zürich, Fermi National Accelerator Laboratory, the University of Illinois at Urbana-Champaign, the Institut de Ciències de l’Espai (IEEC/CSIC), the Institut de Física d’Altes Energies, Lawrence Berkeley National Laboratory, the Ludwig-Maximilians Universität München and the associated Excellence Cluster Universe, the University of Michigan, the National Optical Astronomy Observatory, the University of Nottingham, The Ohio State University, the University of Pennsylvania, the University of Portsmouth, SLAC National Accelerator Laboratory, Stanford University, the University of Sussex, Texas A&M University, and the OzDES Membership Consortium.

Based in part on observations at Cerro Tololo Inter-American Observatory, National Optical Astronomy Observatory, which is operated by the Association of Universities for Research in Astronomy (AURA) under a cooperative agreement with the National Science Foundation.

The DES data management system is supported by the National Science Foundation under Grant Numbers AST-1138766 and AST-1536171. The DES participants from Spanish institutions are partially supported by MINECO under grants AYA2015-71825, ESP2015-66861, FPA2015-68048, SEV-2016-0588, SEV-2016-0597, and MDM-2015-0509, some of which include ERDF funds from the European Union. IFAE is partially funded by the CERCA program of the Generalitat de Catalunya. Research leading to these results has received funding from the European Research Council under the European Union’s Seventh Framework Program (FP7/2007-2013) including ERC grant agreements 240672, 291329, and 306478. We acknowledge support from the Brazilian Instituto Nacional de Ciência e Tecnologia (INCT) e-Universe (CNPq grant 465376/2014-2).

This manuscript has been authored by Fermi Research Alliance, LLC under Contract No. DE-AC02-07CH11359 with the U.S. Department of Energy, Office of Science, Office of High Energy Physics.

REFERENCES

- Abbott, T. M. C., Abdalla, F. B., Alarcon, A., et al. 2018, *PhRvD*, 98, 043526
- Albert, A., Anderson, B., Bechtol, K., et al. 2017, *ApJ*, 834, 110
- Astropy Collaboration, Robitaille, T. P., Tollerud, E. J., et al. 2013, *A&A*, 558, A33

⁴ <http://www.astropy.org>

- Astropy Collaboration, Price-Whelan, A. M., Sipőcz, B. M., et al. 2018, *AJ*, 156, 123
- Bassino, L. P., Muzzio, J. C., & Rabolli, M. 1994, *ApJ*, 431, 634
- Bechtol, K., Drlica-Wagner, A., Balbinot, E., et al. 2015, *ApJ*, 807, 50
- Bertin, E. 2010, *SWarp: Resampling and Co-adding FITS Images Together*, , ascl:1010.068
- Bressan, A., Marigo, P., Girardi, L., et al. 2012, *MNRAS*, 427, 127
- Brown, T. M., Tumlinson, J., Geha, M., et al. 2014, *ApJ*, 796, 91
- Bullock, J. S., & Boylan-Kolchin, M. 2017, *ARA&A*, 55, 343
- Caldwell, N., Walker, M. G., Mateo, M., et al. 2017, *ApJ*, 839, 20
- Carlin, J. L., Sand, D. J., Muñoz, R. R., et al. 2017, *AJ*, 154, 267
- Chabrier, G. 2003, *PASP*, 115, 763
- Chambers, K. C., Magnier, E. A., Metcalfe, N., et al. 2016, arXiv e-prints, arXiv:1612.05560
- Conn, B. C., Jerjen, H., Kim, D., & Schirmer, M. 2018a, *ApJ*, 852, 68
- . 2018b, *ApJ*, 857, 70
- Crnojević, D., Sand, D. J., Zaritsky, D., et al. 2016, *ApJL*, 824, L14
- Dark Energy Survey Collaboration, Abbott, T., Abdalla, F. B., et al. 2016, *MNRAS*, 460, 1270
- Dotter, A. 2016, *ApJS*, 222, 8
- Drlica-Wagner, A., Bechtol, K., Rykoff, E. S., et al. 2015, *ApJ*, 813, 109
- Drlica-Wagner, A., Bechtol, K., Allam, S., et al. 2016, *ApJL*, 833, L5
- Drlica-Wagner, A., Bechtol, K., Mau, S., et al. 2019, arXiv e-prints, arXiv:1912.03302
- . 2020, *ApJ*, 893, 47
- Flaugher, B., Diehl, H. T., Honscheid, K., et al. 2015, *AJ*, 150, 150
- Forbes, D. A., Bastian, N., Gieles, M., et al. 2018, *Proceedings of the Royal Society of London Series A*, 474, 20170616
- Foreman-Mackey, D., Hogg, D. W., Lang, D., & Goodman, J. 2013, *PASP*, 125, 306
- Frenk, C. S., & White, S. D. M. 2012, *Annalen der Physik*, 524, 507
- Homma, D., Chiba, M., Okamoto, S., et al. 2016, *ApJ*, 832, 21
- Jerjen, H., Conn, B., Kim, D., & Schirmer, M. 2018, arXiv e-prints, arXiv:1809.02259
- Ji, A. P., Simon, J. D., Frebel, A., Venn, K. A., & Hansen, T. T. 2019, *ApJ*, 870, 83
- Kim, D., Jerjen, H., Geha, M., et al. 2016, *ApJ*, 833, 16
- Koposov, S. E., Belokurov, V., Torrealba, G., & Evans, N. W. 2015, *ApJ*, 805, 130
- Li, T. S., Simon, J. D., Kuehn, K., et al. 2018, *ApJ*, 866, 22
- Luque, E., Queiroz, A., Santiago, B., et al. 2016, *MNRAS*, 458, 603
- Luque, E., Santiago, B., Pieres, A., et al. 2018, *MNRAS*, 478, 2006
- Martin, N. F., de Jong, J. T. A., & Rix, H.-W. 2008, *ApJ*, 684, 1075
- Martin, N. F., Ibata, R. A., Chapman, S. C., Irwin, M., & Lewis, G. F. 2007, *MNRAS*, 380, 281
- Martínez-Vázquez, C. E., Vivas, A. K., Gurevich, M., et al. 2019, *MNRAS*, 490, 2183
- Mau, S., Cerny, W., Pace, A. B., et al. 2019, arXiv e-prints, arXiv:1912.03301
- McLeod, B., Geary, J., Ordway, M., et al. 2006, in *Astrophysics and Space Science Library*, ed. J. E. Beletic, J. W. Beletic, & P. Amico, Vol. 336, 337
- McLeod, B., Geary, J., Conroy, M., et al. 2015, *PASP*, 127, 366
- Muñoz, R. R., Côté, P., Santana, F. A., et al. 2018, *ApJ*, 860, 65
- Muñoz, R. R., Padmanabhan, N., & Geha, M. 2012, *ApJ*, 745, 127
- Mutlu-Pakdil, B. 2018, in *American Astronomical Society Meeting Abstracts*, Vol. 231, American Astronomical Society Meeting Abstracts #231, 412.03
- Mutlu-Pakdil, B., Sand, D. J., Carlin, J. L., et al. 2018, *ApJ*, 863, 25
- Plummer, H. C. 1911, *MNRAS*, 71, 460
- Sand, D. J., Strader, J., Willman, B., et al. 2012, *ApJ*, 756, 79
- Sawala, T., Frenk, C. S., Fattahi, A., et al. 2015, *MNRAS*, 448, 2941
- Shipp, N., Drlica-Wagner, A., Balbinot, E., et al. 2018, *ApJ*, 862, 114
- Simon, J. D. 2019a, arXiv e-prints, arXiv:1901.05465
- . 2019b, *ARA&A*, 57, 375
- Simon, J. D., & Geha, M. 2007, *ApJ*, 670, 313
- Skrutskie, M. F., Cutri, R. M., Stiening, R., et al. 2006, *AJ*, 131, 1163
- Stetson, P. B. 1987, *PASP*, 99, 191
- . 1994, *PASP*, 106, 250
- The Dark Energy Survey Collaboration. 2005, arXiv e-prints, astro
- Torrealba, G., Belokurov, V., Koposov, S. E., et al. 2018, *MNRAS*, 475, 5085
- Walker, M. G., Mateo, M., Olszewski, E. W., et al. 2016, *ApJ*, 819, 53

Wetzell, A. R., Hopkins, P. F., Kim, J.-h., et al. 2016, *ApJL*,
827, L23
Wheeler, C., Oñorbe, J., Bullock, J. S., et al. 2015, *MNRAS*,
453, 1305
Willman, B., & Strader, J. 2012, *AJ*, 144, 76

Wolf, J., Martinez, G. D., Bullock, J. S., et al. 2010,
MNRAS, 406, 1220
York, D. G., Adelman, J., Anderson, John E., J., et al. 2000,
AJ, 120, 1579